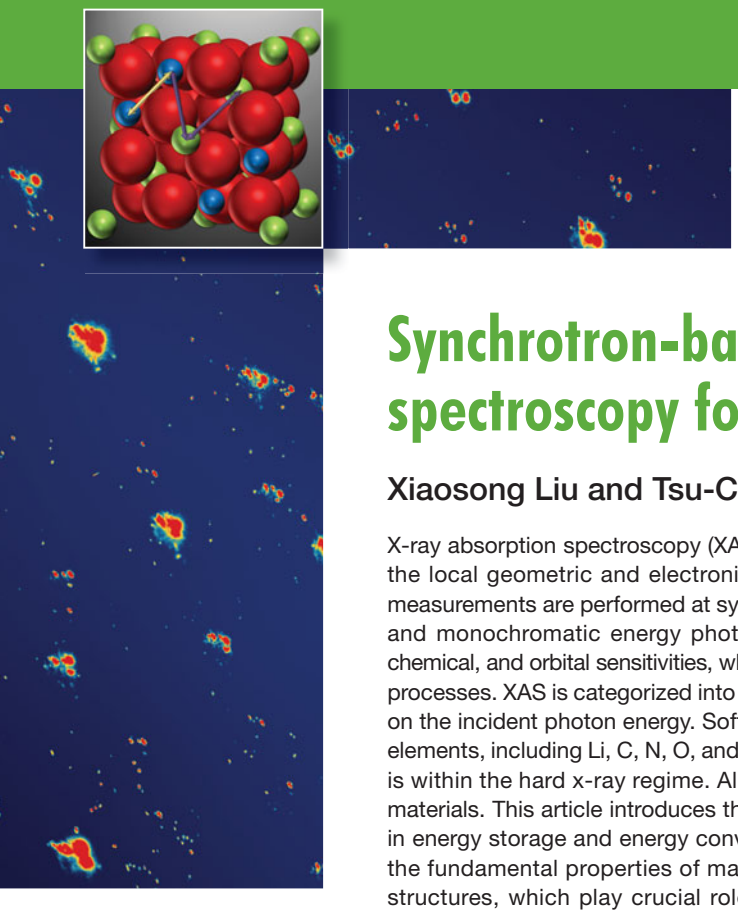

Synchrotron-based x-ray absorption spectroscopy for energy materials

Xiaosong Liu and Tsu-Chien Weng

X-ray absorption spectroscopy (XAS) is a widely used characterization technique to explore the local geometric and electronic structures of materials with element specificity. XAS measurements are performed at synchrotron radiation sources that provide brilliant, tunable, and monochromatic energy photons. The advantages of XAS include good elemental, chemical, and orbital sensitivities, which all stem from inherent electron excitation and transition processes. XAS is categorized into soft (<2000 eV) and hard (>5000 eV) x-ray regimes, based on the incident photon energy. Soft x-rays can probe the K-edges of low-*Z* (atomic number) elements, including Li, C, N, O, and F, and the L-edges of 3*d* transition metals, whose K-edge is within the hard x-ray regime. All of these elements are essential components of energy materials. This article introduces the principle of XAS and reviews some recent applications in energy storage and energy conversion, illustrating the capabilities of XAS to investigate the fundamental properties of materials from the points of view of atomic and electronic structures, which play crucial roles in understanding the reaction mechanisms in high-performance devices.

Introduction

The rapid growth in global fossil-fuel consumption, along with the consequent threat of CO_2 emission and pollution, impose urgent needs for alternative renewable and sustainable energy resources, as well as devices to convert them to electricity. In addition, the intermittent nature of some resources, such as wind and solar energy, motivates the development of effective energy-storage systems. Energy conversion and energy-storage devices transform energies between different formats through a series of chemical, photochemical, electrochemical, or thermoelectrical reactions. These reactions usually involve complex, dynamic, and interrelated processes, such as charge transport, chemical bond forming and breaking, molecular adsorption, surface reconstruction, and phase transformation. The development of characterization tools to observe and capture these phenomena is a prerequisite to gain insights into the mechanisms of chemical and physical reactions and to ultimately make the necessary breakthroughs in energy technologies.

X-ray absorption spectroscopy (XAS) is a powerful technique for studying materials with atomic precision as it directly probes the probability of the transition between atomic energy levels. The x-ray attenuation length depends on the photon energy and the associated x-ray cross section of the material; for 3*d* transition metals, this is a few hundreds of nanometers at L-edges and a few micrometers at K-edges. This probing-depth disparity allows one to probe the surface of a sample with soft x-rays and the bulk of the specimen with hard x-rays. The bulk-probing capability is a useful asset in research on energy materials, allowing direct study of samples under various environments and conditions (such as gas, liquid, solid phases and the interfaces between them, cryogenic/elevated temperatures, vacuum, high pressure, *in situ*/*ex situ*).[1]

This article introduces the principle of XAS and illustrates how XAS has been utilized in studies on energy storage, such as in Li-ion and Li-S batteries, and for energy conversion, including CO_2 reduction and water oxidation. The latter topic usually involves catalysts and the reactions taking place at gas–solid or liquid–solid interfaces. Examples were chosen to illustrate the capability and importance of *in situ* XAS.

Principle of XAS

XAS[2,3] measures the absorption of x-ray photons by a material as a function of x-ray energy, *E*. As depicted in **Figure 1**a, the absorption of x-rays results in the excitation of electrons from a core level of a particular atom to the unoccupied states, leaving behind a core hole. An XAS spectrum, which is the plot of absorption coefficient as a function of *E*, such as the

Xiaosong Liu, State Key Laboratory of Functional Materials for Informatics, Shanghai Institute of Microsystem and Information Technology, Chinese Academy of Sciences, China; xliu3@mail.sim.ac.cn
Tsu-Chien Weng, Center for High Pressure Science & Technology Advanced Research, China; tsuchien.weng@hpstar.ac.cn
doi:10.1557/mrs.2016.113

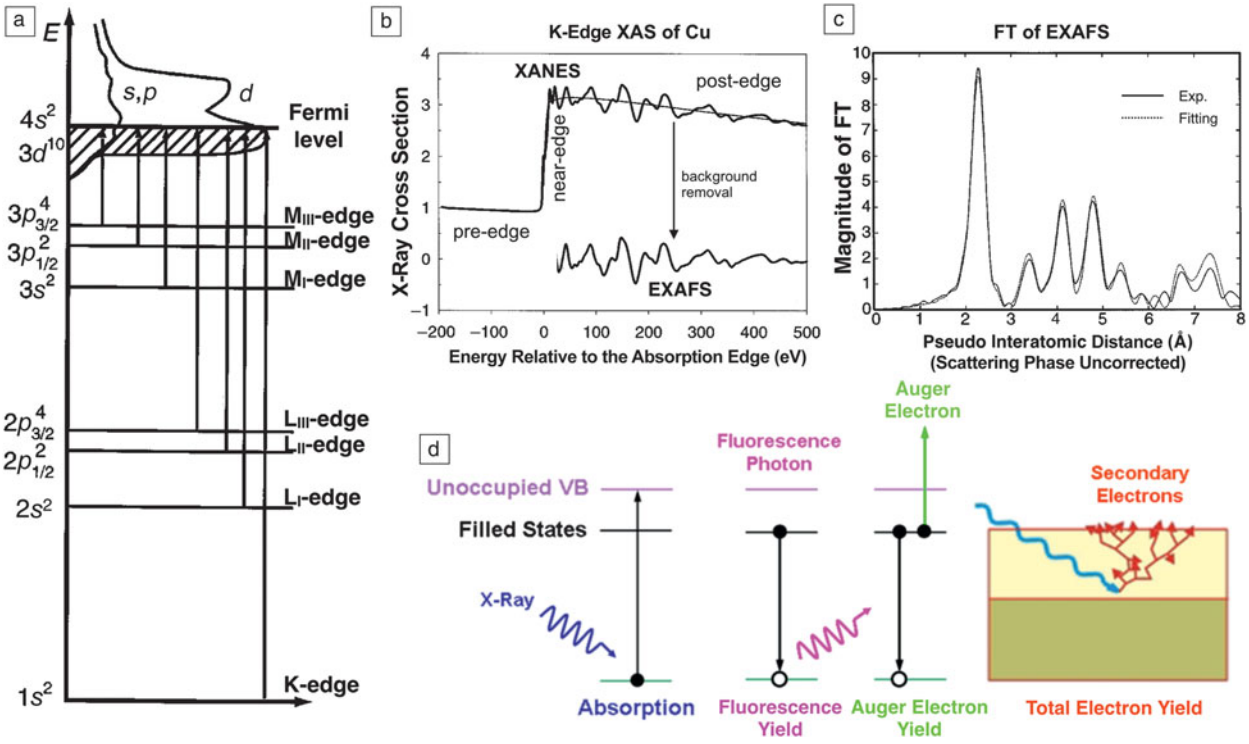

Figure 1. (a) Schematic of x-ray absorption edges. (b) The pre-, near-, and post-edges of the x-ray absorption spectroscopy (XAS) spectrum with extended x-ray absorption fine structure (EXAFS) spectrum after background removal. (c) The Fourier transform (FT) of the EXAFS spectrum represents the pseudo radial distribution function from the photon-absorbing atom to the neighboring atoms. (d) The deexcitation processes lead to three detection modes of XAS: fluorescence yield, Auger electron yield, and total electron yield. Reproduced with permission from Reference 2. © 2011 American Physical Society. Note: *E*, energy; XANES, x-ray absorption near-edge structure; VB, valence band.

one shown in Figure 1b, has three regions: (1) the pre-edge, where E is smaller than the binding energy of a core electron; (2) the absorption-edge, which is typically within ~30 eV above the absorption edge and (termed the x-ray absorption near-edge structure [XANES]) is typically for hard x-rays and near-edge x-ray absorption fine structure for soft x-rays; and (3) the post-edge, termed the extended x-ray absorption fine structure (EXAFS), which is usually ~30 eV beyond the absorption edge. EXAFS corresponds to the oscillating (or wiggling) parts of the spectrum above the absorption edge, resulting from the multiple scattering of an outgoing photoelectron wave from the central excited atom by its surrounding atoms, therefore providing precise information about the local atomic structure (Figure 1c).

XAS measurements record the incident and transmitted x-ray beams through the sample. For soft x-rays (<2000 eV), the sample thickness needs to be extremely thin to match the small attenuation length (<<1 μm), which leads to experimental and instrumental challenges. Alternatively, one can measure x-ray absorption indirectly, as shown in Figure 1d, by detecting decay products of the created core hole, such as fluorescence yield (FY), Auger electron yield (AEY), or total electron yield (TEY). All of these decay products are approximately proportional to the number of core holes created in the absorption process with varied probing depths. AEY detection records the elastically scattered Auger electrons and provides the best surface sensitivity. TEY is dominated by inelastically scattered secondary electrons, and its probing depth has been estimated to be in the range of 5 nm for metals and semiconductors and slightly larger for insulators. FY detection probes deeper because of the longer mean free path of the emitted photons in a material (typically 100 nm to several μm, depending on the absorption length at the photon energy of the emitted photons). By simultaneously measuring electron and fluorescence yields, one can obtain a coarse depth profile of the sample.

Applications of XAS in energy storage

Though they have revolutionized portable electronics technology, present lithium-ion battery technologies still face key challenges in terms of stability, safety, capacity, and cost for wider applications in electric vehicles and other large-scale energy storage. Thus, they have attracted intense research attention and effort.[4,5] XAS has been extensively used as an incisive characterization tool to study battery materials. Several applications are discussed here.

Transition-metal cathodes of lithium-ion batteries

The charge and discharge process of a 3*d* transition-metal-based intercalation cathode involves the evolution of both atomic and electronic structures.[6–8] This is where XAS, in both

the soft and hard x-ray regime, becomes important.[9–11] XAS has been employed to investigate cathode materials and has provided valuable information, including the oxidation states of metal ions, site symmetries, and covalent bond strength.

This is illustrated by a comprehensive study on $LiCo_{1/3}Ni_{1/3}Mn_{1/3}O_2$.[12] **Figure 2**a–c shows the XAS spectra at Mn, Co, and Ni K-edges. In the pre-edge region, as magnified in the inset in each panel, the small hump is the dipole-forbidden 1*s* to 3*d* transition, gaining intensity from the metal 3*d*–4*p* mixing or metal-3*d*–ligand-2*p* mixing under one-electron orbital approximation. The main absorption peak is the dipole-allowed 1*s* to 4*p* transition, and a shoulder on the lower energy side is attributed to the ligand-to-metal charge transfer. The entire edge shift is normally considered as an indicator for the change of the oxidation state of the metal ions. In Figure 2c, it is clear that Ni increases the oxidation state during battery charging, because the edge shifts to a higher energy. No such clear shift is observed for Mn and Co.

It is impossible to determine the change in the oxidation state only by the edge feature, since many other factors would also affect it. In this respect, metal L-edge XAS in the soft x-ray region has an advantage, because it directly probes the unoccupied 3*d* states through the dipole-allowed 2*p*-to-3*d* transition. As shown in Figure 2g–i, the L-edge spectra consist of sharp peaks with high intensity in two regions (L_{III} and L_{II}), resulting from the core–hole spin–orbital coupling. The multiplet structure in the L_{III}-edge is a fingerprint of different oxidation states of metal ions. It is obvious that Mn and Co remain mostly unchanged in Mn^{4+} and Co^{2+} states at different states of charge, while Ni^{2+} increases to Ni^{4+} with delithiation.

This is further confirmed by the metal K-edge EXAFS measurements from the point of view of atomic structure, as shown in Figure 2d–f. The EXAFS peak features are sensitive to the variation of atoms in different coordination shells. The significant change in the first peak intensity in the Ni spectra indicates a decrease in the Ni–O bond length and the occurrence of charge compensation at the Ni sites. All other bond lengths can be calculated from quantitative analysis of EXAFS measurements. Many other important properties of cathodes, such as phase transformation, metal-*d*–ligand-*p* hybridization, and local structure distortion, have also been studied with XAS.[11,13–15]

Solid-electrolyte interface of lithium-ion batteries

The solid-electrolyte interface (SEI) is a Li^+-conducting but electron-insulating layer between an electrode and the electrolyte in lithium-ion batteries. It forms mostly during the first several cycles, resulting from the degradation of a small amount of organic electrolyte triggered by electrolyte reduction/oxidation at the cathode/anode, respectively. The SEI acts as a passivation layer to prevent continuous electrolyte degradation and lithium consumption during cycling. Although the SEI has been explored for almost 40 years, it remains a not well-understood phenomenon. A better understanding of the mechanism of formation is critical for optimizing the combination of electrolyte–electrode and improving the efficiency, stability, and lifetime of lithium-ion batteries.[16]

The SEI contains a variety of decomposition products from the electrolyte and dissolution or contamination products from electrodes, which consist of 3*d* transition-metal and low-*Z* elements (where *Z* is the atomic number), such as C, Si, N, O, and F. The absorption edges of all of these "light" atoms are within the energy regime of soft x-rays. Balasubramanian et al.[17] studied the formation of the SEI at different cycling temperatures on $Li(Ni_xCo_{1-x})O_2$ cathode surfaces by XAS at L-edges of Ni and Co, and at K-edges of F and O. They found that the SEI mainly contained poly(vinylidene fluoride) (PVDF) and LiF. By fitting the F K-edge XAS spectrum of the SEI with linear combinations of standard PVDF and LiF spectra, they could further estimate the percentage of each component in the SEI under different cycling conditions. While the PVDF was the electrode binder and remained intact during cycling, LiF was considered the decomposition product of the $LiPF_6$ electrolyte. Delacourt et al.[18] investigated the effect of manganese contamination on the SEI properties on a model anode surface. The Mn L-edge XAS indicated the presence of Mn^{2+} ions in the SEI films. A multiphase transformation process was proposed, where Mn^{2+} from the electrolyte was first reduced to Mn^0 at the electrode surface and further reoxidized back to Mn^{2+} by reacting with solvent molecules.

Beyond Li-ion batteries

The capacity of Li-ion batteries is still not high enough to satisfy the current requirements for electrical transportation and stationary electricity storage. Novel electrochemistry and materials beyond Li-ion batteries are urgently demanded;[19] in particular, Li-air and Li-S batteries have attracted extensive research interest.[20–22] One important issue in Li-air batteries is the catalyst for the oxygen-reduction (ORR) and oxygen-evolution reactions (OER) taking place at the interface of the electrodes and the aqueous/nonaqueous electrolyte. The applications of XAS in this field are discussed along with catalysts for CO_2 reduction and water oxidation reactions in the next section.

The biggest obstacle to the Li-S battery involves high dissolution of polysulfides and its shuttling to the anode during the discharge process. To overcome this, various materials, such as polymers and C/S nanocomposites, have been used to immobilize S and Li polysulfides. Ji et al. synthesized a nanocomposite of graphene oxide with a sulfur-coating (GO-S) as the cathode material for Li-S batteries.[23] With a low-temperature heat treatment, some functional groups, such as epoxy and hydroxyl, still remained on graphene oxide (GO) (**Figure 3**a). These functional groups enhanced the binding of S in the composite cathode and improved the reversibility, capacity stability, and rate capability of the Li-S battery.

The mechanism of anchoring S is revealed by C K-edge XAS, as shown in Figure 3b. Two variations are observed in the spectra of GO and GO-S nanocomposites. The first is the peaks at A and D that correspond to the transition of the C 1*s* core electron to the π* state and the excitonic state, respectively,

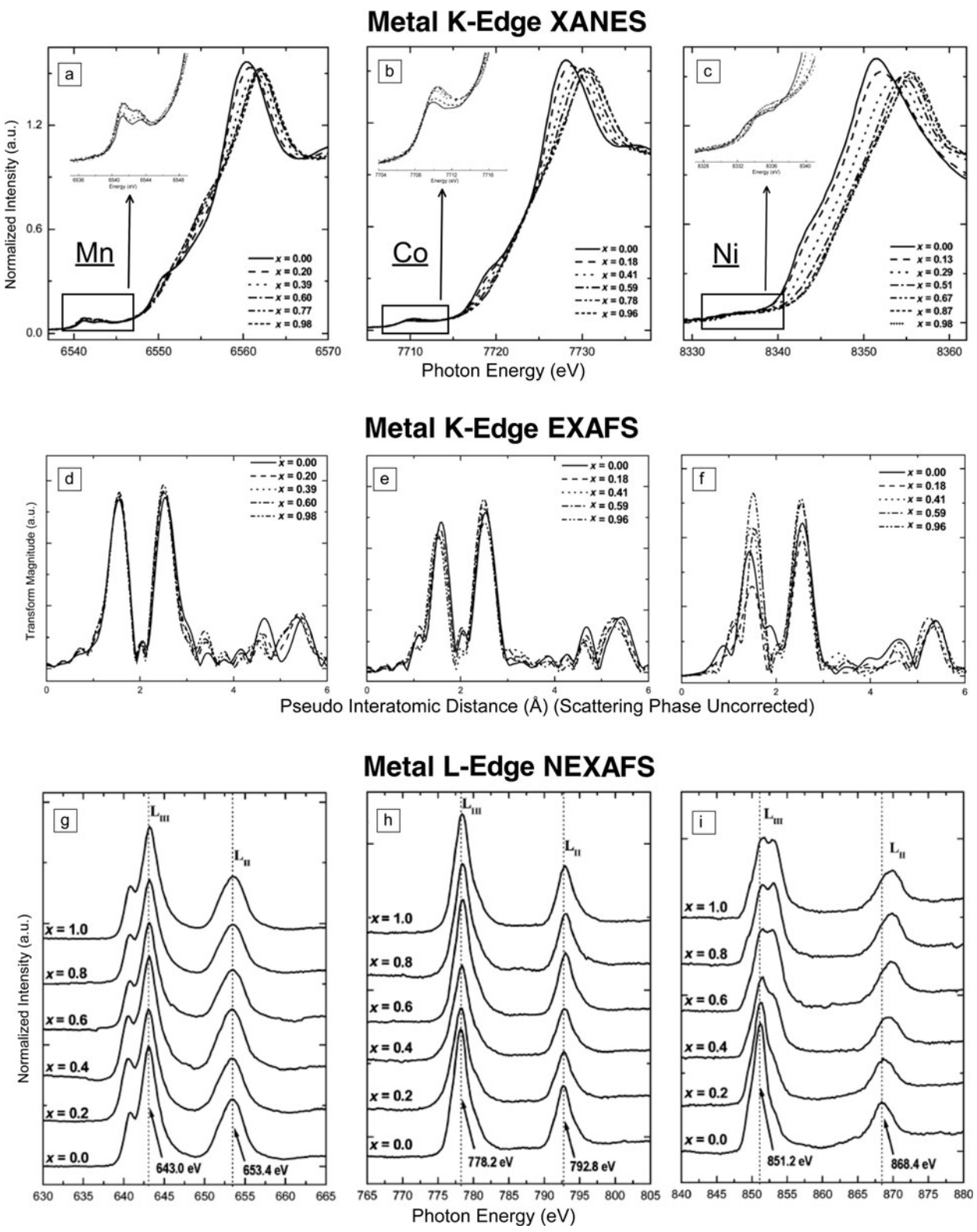

Figure 2. (a–c) Metal (Mn, Co, Ni) K-edge x-ray absorption near-edge structure (XANES), (d–f) metal K-edge extended x-ray absorption fine structure (EXAFS), (g–i) metal L-edge near-edge x-ray absorption fine structure (NEXAFS) spectra of $Li_{1-x}Co_{1/3}Ni_{1/3}Mn_{1/3}O_2$. The spectral changes in Ni K-edge XANES and L-edge NEXAFS and the decrease in Ni–O bond length in EXAFS indicate that Ni^{2+} increases to Ni^{4+} during battery charging, while Mn and Co remain mostly unchanged as Mn^{4+} and Co^{2+}. Reproduced with permission from Reference 12.

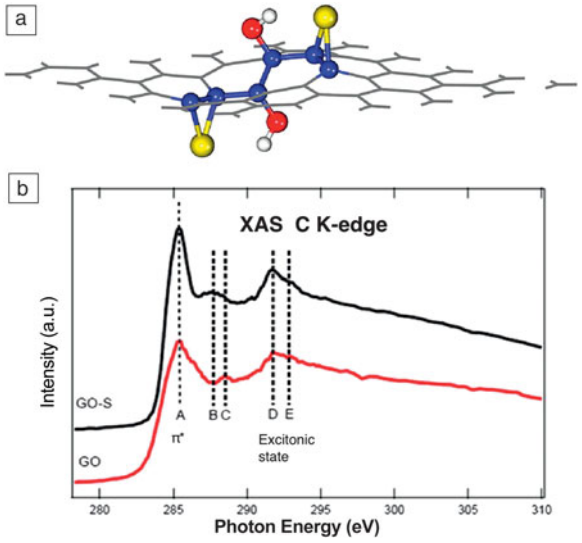

Figure 3. (a) Representative pattern of graphene oxide (GO) immobilizing S. The hydroxyl enhances the binding of S to the C=C bond. Yellow, red, and white balls denote S, O, and H atoms, respectively. Others are C atoms. (b) C K-edge x-ray absorption spectroscopy (XAS) spectra of GO and GO with a sulfur coating (GO-S) nanocomposites after heat treatment in Ar at 155°C for 12 h. The enhanced transition to the π^* state and the excitonic state in GO-S indicates that the incorporated S improves the ordering of the sp^2-hybridized carbon structure. Adapted with permission from Reference 25. © 2011 American Chemical Society.

which become sharper in GO-S. This indicates that the incorporated S improves the ordering of the sp^2-hybridized carbon structure. The other change is that the peak C weakened significantly along with the appearance of a new peak B after S was doped into GO. It is evident that the C–O bond in functional groups on the GO surface is reduced, and a strong chemical interaction between incorporated S species with GO forms C–S bonds. XAS spectroscopy with verification by theoretical simulations thus provides valuable information for better understanding variations in material properties and the mechanism of interactions in complicated composites.

Applications of XAS in energy conversion

Energy conversion is a dynamic process. *In situ* studies to investigate the system at work when the catalysts are under operating conditions are crucial. For catalysts with homogeneities in composition and geometry, the common practice is to fit the *in situ* XAS spectra of the catalysts with a linear combination of known standards to deduce the species distribution along the reaction pathways. When catalysts have more than one geometrical site, one needs to identify the active catalytic site before further study to elucidate the reaction mechanism.

The objective behind doping or interfacing the catalysts with other metals is to tune the catalytic activity by modifying the electronic or geometrical structure of the target catalysts. It is essential to distinguish and identify the affecting factors, in terms of electronic and geometrical structures, for the active catalysts to provide the foundation for rational design of better catalysts.

Electrocatalytic CO_2 reduction by Cu/Au(111) monolayer

Anthropogenic CO_2 poses a serious threat to humanity as a greenhouse gas. It could become a major resource if an economically feasible technology is found for its conversion to liquid fuels and feedstock chemicals. The existing technologies[24] for this are energy intensive. A suitable catalyst can reduce the energetic barrier for CO_2 reduction to an organic. Thus, it is important to understand the interaction between CO_2 molecules and the catalyst from the viewpoint of the electronic structure surrounding the catalytic center.

Compared to metal electrodes that require large overpotentials (~1 V) for the conversion of CO_2 to a hydrocarbon without selectivity over H_2 evolution,[25] Cu/Au alloys were reported to have improved faradaic efficiencies for CO_2 reduction. Friebel et al.[26] investigated the electronic structures of a Cu monolayer (ML) and of Cu multilayers on Au(111) substrates in alkaline solution using *in situ* high-energy-resolution fluorescence-detection x-ray absorption spectroscopy (HERFD XAS,[27,28] see **Figure 4**c for setup scheme). One can apply the "bond-length-with-a-ruler" concept[29,30] to rectify

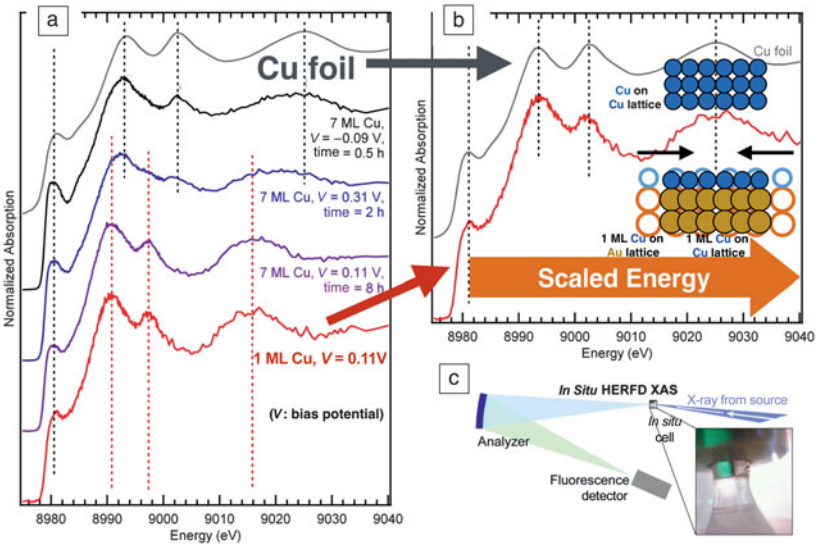

Figure 4. (a) *In situ* high-energy-resolution fluorescence-detection x-ray absorption spectroscopy (HERFD XAS) of Cu/Au(111). (b) Comparison of XAS for Cu foil and one monolayer (ML) Cu/Au(111) onto the scaled axis based on the "bond-length-with-a-ruler" concept. (c) HERFD XAS setup. The Cu ML on the Au(111) substrate is in the metallic state. Reproduced with permission from Reference 33. © 2014 American Chemical Society.

the scattering phase difference between 1 ML Cu/Au(111) and Cu/"Cu" (bulk Cu), resulting from different lattice constants of the substrates (d_{Au} = 2.88 Å versus d_{Cu} = 2.56 Å). The *in situ* HERFD XAS spectrum of 1 ML Cu/Au(111) with rescaled energy axis aligns profoundly with that of bulk Cu (Figure 4b). This indicates the Cu ML on the Au(111) substrate is in the metallic state.

The significant tensile strain of a single Cu ML on Au alters the redox behavior of Cu. This provides another parameter dimension in designing new catalysts by "tuning" the interaction between the strained Cu surface and the reaction to control the product selectivity.

Distinguishing sites in (Ni,Fe)OOH for water electrolysis

A water-oxidation catalyst with low overpotential for the OER is desirable for use as the anode in electrochemical and photoelectrochemical cells. To rectify the performance loss resulting from the high overpotential of existing OER catalysts, one would have to use high-bandgap photoabsorbers or increase catalyst loading to match the catalytic current density[31] and geometric photocurrent. Among mixed-metal oxides composed of earth-abundant elements, a mixed Ni-Fe compound is the most promising OER catalyst in an alkaline electrolyte. The addition of Fe to NiOOH results in a 500-fold higher OER activity,[32] compared to pure Ni and Fe oxyhydroxide parent compounds. One can use *in situ* HERFD XAS to probe the local electronic structure at Ni and Fe sites, over the full range of the Fe/Ni ratio at potentials below and during OER conditions, to understand the correlation between the catalytic activity and the composition of Ni and Fe sites within the catalysts.

EXAFS data[32] show changes both in the Fe–O and Ni–O bond lengths with increasing applied potential. There are two types of Ni sites, characterized as α-$Ni(OH)_2$ and γ-NiOOH. A strong correlation found between nearest metal–metal distances in Ni and Fe K-edge EXAFS data indicated that Fe substitutes for Ni in both Ni sites. In addition, Fe and Ni K-edge EXAFS show collinear Fe-Ni-Ni, Ni-Fe-Ni, and Ni-Ni-Ni arrangements, indicating that Fe is not intercalated between the hexagonal [NiO_2] sheets, but instead substitutes for Ni within the sheets.

Identifying the active site in spinel Co_3O_4 for water oxidation

XAS is an averaging technique, which means the collected spectrum is a superposition of x-ray absorption of all probed elements. If there is more than one site in a catalyst, one can either use distinct spectral features between the sites, resulting from differences in charge, spin,[33,34] or geometry, or substitute a specific site with a different inert element to collect site-selective XAS. Accordingly, the active site of the catalyst can be deduced and identified from site-selective XAS combining with the corresponding catalytic activities.

Spinel cobalt oxide (Co_3O_4) is an efficient OER catalyst,[35–37] with activity competitive with and comparable to noble metal-based catalysts. There are two geometrical sites in Co_3O_4 with different oxidation states: one divalent ion at the tetrahedral site (Co^{2+}_{Td}, green balls in **Figure 5**a) and two trivalent ions at the octahedral site (Co^{3+}_{Oh}, blue balls in Figure 5a). H.M. Chen and Liu et al.[38] used catalytically inactive Zn^{2+} and Al^{3+} to replace Co^{2+}_{Td} and Co^{3+}_{Oh}, respectively, to disclose the identity of the OER active site. *In situ* EXAFS data (Figure 5b) showed that both substituted cobalt oxides, $ZnCo_2O_4$ and $CoAl_2O_4$, maintain the cubic-spinel structure as that of the pure Co_3O_4.

Throughout electrolysis, the principal absorption maximum (Figure 5c) of the Co K-edge XANES remained constant for $CoAl_2O_4$, but kept increasing for $ZnCo_2O_4$ as the applied positive bias increased. This indicates that positive charge accumulates on cobalt ions in $CoAl_2O_4$ under an applied bias, promoting the affinity to oxygen ions on the catalyst surfaces to form cobalt oxyhydroxide (CoOOH).

These findings from the x-ray spectroscopy study[38] disclose that Co^{2+}_{Td} is the active species in Co_3O_4 for OER, releasing electrons under applied positive bias.

Conclusion and prospective

In this article, we reviewed applications of XAS[39] to recent progress in research on rechargeable batteries and energy conversion of CO_2 and H_2O. One can apply XAS to extract the oxidation state information from XANES data, the nearest neighbor distances from EXAFS data, or the electronic and

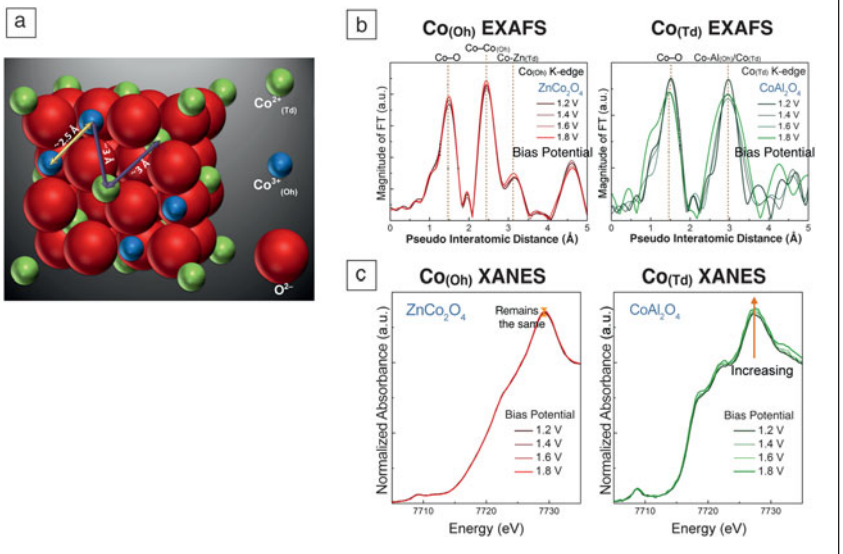

Figure 5. (a) Illustration of Co_3O_4 with divalent tetrahedral (Td) sites in green and trivalent octahedral (Oh) sites in blue. (b) Fourier transform (FT) of extended x-ray absorption fine structure (EXAFS) spectra and (c) x-ray absorption near-edge structure (XANES) spectra of substituted Co_3O_4 as a function of the applied bias potentials. The changes in Co–O bond distance and absorption intensity under oxygen evolution reaction (OER) conditions indicate that $Co^{2+}_{(Td)}$ is the active species in Co_3O_4 for OER. Reproduced with permission from Reference 38. © 2016 American Chemical Society.

geometrical structure changes at the reactive sites with varying probing depth or under *in situ* conditions. In short, XAS is a direct and incisive tool to probe the electronic structure of energy materials and offers site valence, site symmetry, and spin information.

Recent technical developments in sample environments allow us to study the system at work, investigating energy materials and model devices under semirealistic, and *operando* conditions. Technical advancements in instrumentation enable the examination of liquid–solid interfaces,[40] where the chemical transformation occurs (e.g., charge transport, energy transport, chemical bond breaking, and formation).

Other x-ray spectroscopic techniques not discussed here include x-ray emission spectroscopy (XES) and inelastic x-ray scattering,[41–46] in nonresonant and resonant modes. In a simplified one-electron orbital picture, XAS probes the unoccupied molecular orbitals, and XES probes the occupied ones. Among other valence-shell information, molecular orbital hybridization[47–54] is one of the unique properties that can be probed directly by XES. For example, valence-to-core resonant inelastic x-ray scattering was used to determine that CO is adsorbed on the top of one Pt atom instead of bridging between Pt atoms.[47] This article demonstrated that x-ray spectroscopy is a unique tool to unveil the electronic structure details and provide in-depth insights into the functionality and properties of energy materials.

Acknowledgments

This work was supported by the National Natural Science Foundation of China (21473235, 11227902), One Hundred Person Project of the Chinese Academy of Sciences, Shanghai Pujiang Program (14PJ1410400), and NSAF (U1530402).

References

1. K.-D. Liss, A. Bartels, A. Schreyer, H. Clemens, *Textures Microstruct.* **35**, 219 (2003).
2. J.J. Rehr, R.C. Albers, *Rev. Mod. Phys.* **72**, 621 (2000).
3. F de Groot, A. Kotani, *Core Level Spectroscopy of Solids* (Taylor & Francis, Hoboken, NJ, 2008).
4. M. Armand, J.M. Tarascon, *Nature* **451**, 652 (2008).
5. J.B. Goodenough, K.-S. Park, *J. Am. Chem. Soc.* **135**, 1167 (2013).
6. K. Mizushima, P.C. Jones, P.J. Wiseman, J.B. Goodenough, *Mater. Res. Bull.* **15**, 783 (1980).
7. A.K. Padhi, K.S. Nanjundaswamy, J.B. Goodenough, *J. Electrochem. Soc.* **144**, 1188 (1997).
8. M.M. Thackeray, P.J. Johnson, L.A. Depicciotto, P.G. Bruce, J.B. Goodenough, *Mater. Res. Bull.* **19**, 179 (1984).
9. W.-S. Yoon, K.Y. Chung, K.-H. Oh, K.-B. Kim, *J. Power Sources* **119–121**, 706 (2003).
10. W.-S. Yoon, K.-B. Kim, M.G. Kim, M.-K. Lee, H.J. Shin, J.-M. Lee, J.-S. Lee, C.-H. Yo, *J. Phys. Chem. B* **106**, 2526 (2002).
11. X. Liu, J. Liu, R. Qiao, Y. Yu, H. Li, L. Suo, Y. Hu, Y. Chuang, G. Shu, F. Chou, T. Weng, D. Nordlund, D. Sokaras, Y. Wang, H. Lin, B. Barbiellini, A. Bansil, X. Song, Z. Liu, S. Yan, G. Liu, S. Qiao, T.J. Richardson, D. Prendergast, Z. Hussain, F.M.F. de Groot, W. Yang, *J. Am. Chem. Soc.* **134**, 13708 (2012).
12. W.-S. Yoon, M. Balasubramanian, K.Y. Chung, X.-Q. Yang, J. McBreen, C.P. Grey, D.A. Fischer, *J. Am. Chem. Soc.* **127**, 17479 (2005).
13. W. Yang, X. Liu, R. Qiao, P. Olalde-Velasco, J.D. Spear, L. Roseguo, J.X. Pepper, Y.-D. Chuang, J.D. Denlinger, Z. Hussain, *J. Electron. Spectrosc. Relat. Phenom.* **190**, 64 (2013).
14. R. Qiao, Y. Wang, P. Olalde-Velasco, H. Li, Y.-S. Hu, W. Yang, *J. Power Sources* **273**, 1120 (2014).
15. Y.-N. Zhou, J. Ma, E. Hu, X. Yu, L. Gu, K.-W. Nam, L. Chen, Z. Wang, X.-Q. Yang, *Nat. Commun.* **5**, 5381 (2014).
16. M. Gauthier, T.J. Carney, A. Grimaud, L. Giordano, N. Pour, H.-H. Chang, D.P. Fenning, S.F. Lux, O. Paschos, C. Bauer, F. Maglia, S. Lupart, P. Lamp, Y. Shao-Horn, *J. Phys. Chem. Lett.* **6**, 4653 (2015).
17. M. Balasubramanian, H.S. Lee, X. Sun, X.Q. Yang, A.R. Moodenbaugh, J. McBreen, D.A. Fischer, Z. Fu, *Electrochem. Solid-State Lett.* **5**, A22 (2002).
18. C. Delacourt, A. Kwong, X. Liu, R. Qiao, W.L. Yang, P. Lu, S.J. Harris, V. Srinivasan, *J. Electrochem. Soc.* **160**, A1099 (2013).
19. P.G. Bruce, S.A. Freunberger, L.J. Hardwick, J.-M. Tarascon, *Nat. Mater.* **11**, 19 (2011).
20. Y. Cui, A. Abouimrane, J. Lu, T. Bolin, Y. Ren, W. Weng, C. Sun, V.A. Maroni, S.M. Heald, K. Amine, *J. Am. Chem. Soc.* **135**, 8047 (2013).
21. T.A. Pascal, K.H. Wujcik, J. Velasco-Velez, C. Wu, A.A. Teran, M. Kapilashrami, J. Cabana, J. Guo, M. Salmeron, N. Balsara, D. Prendergast, *J. Phys. Chem. Lett.* **5**, 1547 (2014).
22. K.H. Wujcik, J. Velasco-Velez, C.H. Wu, T. Pascal, A.A. Teran, M.A. Marcus, J. Cabana, J. Guo, D. Prendergast, M. Salmerón, N.P. Balsara, *J. Electrochem. Soc.* **161**, A1100 (2014).
23. L. Ji, M. Rao, H. Zheng, L. Zhang, Y. Li, W. Duan, J. Guo, E.J. Cairns, Y. Zhang, *J. Am. Chem. Soc.* **133**, 18522 (2011).
24. G. Centi, S. Perathoner, *Catal. Today* **148**, 191 (2009).
25. K.P. Kuhl, E.R. Cave, D.N. Abram, T.F. Jaramillo, *Energy Environ. Sci.* **5**, 7050 (2012).
26. D. Friebel, F. Mbuga, S. Rajasekaran, D.J. Miller, H. Ogasawara, R. Alonso-Mori, D. Sokaras, D. Nordlund, T.-C. Weng, A. Nilsson, *J. Phys. Chem. C* **118**, 7954 (2014).
27. O.V. Safonova, M. Tromp, J.A. van Bokhoven, F.M.F. de Groot, J. Evans, P. Glatzel, *J. Phys. Chem. B* **110**, 16162 (2006).
28. P. Glatzel, F.M.F. de Groot, O. Manoilova, D. Grandjean, B.M. Weckhuysen, U. Bergmann, R. Barrea, *Phys. Rev. B Condens. Matter* **72**, 014117 (2005).
29. F. Sette, J. Stohr, A.P. Hitchcock, *Chem. Phys. Lett.* **110**, 517 (1984).
30. J. Stohr, F. Sette, A.L. Johnson, *Phys. Rev. Lett.* **53**, 1684 (1984).
31. M.G. Walter, E.L. Warren, J.R. McKone, S.W. Boettcher, Q. Mi, E.A. Santori, N.S. Lewis, *Chem. Rev.* **110**, 6446 (2010).
32. D. Friebel, M.W. Louie, M. Bajdich, K.E. Sanwald, Y. Cai, A.M. Wise, M.-J. Cheng, D. Sokaras, T.-C. Weng, R. Alonso-Mori, R.C. Davis, J.R. Bargar, J.K. Norskov, A. Nilsson, A.T. Bell, *J. Am. Chem. Soc.* **137**, 1305 (2015).
33. T.-J. Kuehn, J. Hormes, N. Matoussevitch, H. Boennemann, P. Glatzel, *Inorg. Chem.* **53**, 8367 (2014).
34. M.M. Grush, G. Christou, K. Hamalainen, S.P. Cramer, *J. Am. Chem. Soc.* **117**, 5895 (1995).
35. H. Tueysuez, Y.J. Hwang, S.B. Khan, A.M. Asiri, P. Yang, *Nano Res.* **6**, 47 (2013).
36. Y. Liang, Y. Li, H. Wang, J. Zhou, J. Wang, T. Regier, H. Dai, *Nat. Mater.* **10**, 780 (2011).
37. F. Jiao, H. Frei, *Angew. Chem. Int. Ed.* **48**, 1841 (2009).
38. H.-Y. Wang, S.-F. Hung, H.-Y. Chen, T.-S. Chan, H.M. Chen, B. Liu, *J. Am. Chem. Soc.* **138**, 36 (2016).
39. G. Bunker, *Introduction to XAFS: A Practical Guide to X-Ray Absorption Fine Structure Spectroscopy* (Cambridge University Press, New York, 2010).
40. J.-J. Velasco-Velez, C.H. Wu, T.A. Pascal, L.F. Wan, J. Guo, D. Prendergast, M. Salmeron, *Science* **346**, 831 (2014).
41. I. Waluyo, D. Nordlund, U. Bergmann, D. Schlesinger, L.G.M. Pettersson, A. Nilsson, *J. Chem. Phys.* **140**, 244506 (2014).
42. D. Sokaras, D. Nordlund, T.C. Weng, R.A. Mori, P. Velikov, D. Wenger, A. Garachtchenko, M. George, V. Borzenets, B. Johnson, Q. Qian, T. Rabedeau, U. Bergmann, *Rev. Sci. Instrum.* **83**, 043112 (2012).
43. A. Nilsson, D. Nordlund, I. Waluyo, N. Huang, H. Ogasawara, S. Kaya, U. Bergmann, L.A. Naeslund, H. Ostrom, P. Wernet, K.J. Andersson, T. Schiros, L.G.M. Pettersson, *J. Electron. Spectrosc. Relat. Phenom.* **177**, 99 (2010).
44. L.A. Naslund, D.C. Edwards, P. Wernet, U. Bergmann, H. Ogasawara, L.G.M. Pettersson, S. Myneni, A. Nilsson, *J. Phys. Chem. A* **109**, 5995 (2005).
45. N. Huang, D. Nordlund, C. Huang, U. Bergmann, T.M. Weiss, L.G.M. Pettersson, A. Nilsson, *J. Chem. Phys.* **135**, 164509 (2011).
46. U. Bergmann, H. Groenzin, O.C. Mullins, P. Glatzel, J. Fetzer, S.P. Cramer, *Pet. Sci. Technol.* **22**, 863 (2004).
47. P. Glatzel, J. Singh, K.O. Kvashnina, J.A. van Bokhoven, *J. Am. Chem. Soc.* **132**, 2555 (2010).
48. J.C. Swarbrick, T.-C. Weng, K. Schulte, A.N. Khlobystov, P. Glatzel, *Phys. Chem. Chem. Phys.* **12**, 9693 (2010).
49. J.C. Swarbrick, Y. Kvashnin, K. Schulte, K. Seenivasan, C. Lamberti, P. Glatzel, *Inorg. Chem.* **49**, 8323 (2010).
50. Y.-T. Tseng, C.-H. Chen, J.-Y. Lin, B.-H. Li, Y.-H. Lu, C.-H. Lin, H.-T. Chen, T.-C. Weng, D. Sokaras, H.-Y. Chen, Y.-L. Soo, T.-T. Lu, *Chem. Eur. J.* **21**, 17570 (2015).
51. T.-T. Lu, T.-C. Weng, W.-F. Liaw, *Angew. Chem. Int. Ed.* **53**, 11562 (2014).
52. C.J. Pollock, S. DeBeer, *J. Am. Chem. Soc.* **133**, 5594 (2011).
53. K.M. Lancaster, K.D. Finkelstein, S. DeBeer, *Inorg. Chem.* **50**, 6767 (2011).
54. M.U. Delgado-Jaime, S. DeBeer, M. Bauer, *Chem. Eur. J.* **19**, 15888 (2013). □